pp 830–846.
doi:10.1017/aer.2020.135

Conceptual design and numerical studies of active flow control aerofoil based on shape-memory alloy and macro fibre composites

W. Zhang
College of Aerospace Science and Engineering
National University of Defense Technology
Changsha
China
and
China Aerodynamics Research and Development Center
Mianyang
China

X.T. Nie, **X.Y. Gao and W.H. Chen**
chenwanhua@cardc.cn
China Aerodynamics Research and Development Center
Mianyang
China

ABSTRACT

Active flow control for aerofoils has been proven to be an effective way to improve the aerodynamic performance of aircraft. A conceptual hybrid design with surfaces embedded with Shape-Memory Alloy (SMA) and trailing Macro Fibre Composites (MFC) is proposed to implement active flow control for aerofoils. A Computational Fluid Dynamics (CFD) model has been built to explore the feasibility and potential performance of the proposed conceptual hybrid design. Accordingly, numerical analysis is carried out to investigate the unsteady flow characteristics by dynamic morphing rather than using classical static simulations and complicated coupling. The results show that camber growth by SMA action could cause an evident rise of C_l and C_d in the take-off/landing phases when the Angle-of-Attack (AoA) is less than 10°. The transient tail vibration behaviour in the cruise period when using MFC actuators is studied over wide ranges of frequency, AoA and vibration amplitude. The buffet frequency is locked in by the vibration frequency, and a decrease of 1.66–2.32% in C_d can be achieved by using a proper vibration frequency and amplitude.

Keywords: Aerodynamics; Active flow control; SMA: MFC; RAE 2822

Received 29 December 2019; revised 12 November 2020; accepted 17 November 2020.

ACRONYMS AND NOMENCLATURE

CFD	Computational fluid dynamics
CAE	Computational structure mechanics
SMA	Shape-memory alloy
MFC	Macro fibre composite
RANS	Reynolds-averaged Navier–Stokes
AoA	Angle-of-attack
A	Vibration amplitude
T	Time
C	Chord length
U_∞	Coming velocity
Re	Reynolds number
C_d	Drag coefficient
C_l	Lift coefficient
C_p	Pressure coefficient
y^+	Y plus wall distance
Ma	Mach number
ω	Angular velocity
f	Vibration frequency
θ	Rotated angle

1.0 INTRODUCTION

For new flight vehicles, higher mobility and adaptability are sought to satisfy the rapidly increasing demand for air transport. For civil aircraft, the aim is to enhance the economic performance and reduce the fuel consumption and exhaust emissions, resulting in strict aircraft design requirements. According to a report by the National Aeronautics and Space Administration (NASA), the payload of an aircraft can be increased by 20–40% by increasing the lift coefficient or reducing the drag coefficient by 5% during take-off[1]. Correspondingly, the payload could be increased by 65% by increasing the lift coefficient by 5% during landing[2,3].

Active flow control technology effectively improves the aerodynamic performance of aircraft and provides a solution to requirements such as reduced noise and emissions and short departure and landing. Researchers have carried out various extensive investigations on active flow control technology, providing deep understanding on the unsteady flow characteristics around the aircraft and resulting in growing maturity of technologies such as smart materials, active control and mechatronics. Smart strategies can be implemented to control the separation phenomenon and thereby enhance the aerodynamic performance, thus improving the economy, mobility and adaptability of the aircraft.

Maldonado used synthetic jet actuators to enhance the performance of wind turbine blades and decrease the vibration by mitigating flow separation[4]. Botez conducted modelling, simulation and control for a miniature electrical actuator integrated into a new morphing

https://doi.org/10.1017/aer.2020.135 Published online by Cambridge University Press

wing application[5]. The disadvantage of the conventional aileron lies in how it changes the camber of the wing. Indeed, the aileron rotates around its hinge point, thus creating a discontinuity in the slope of the aerofoil camber. Wu used linear ultrasonic motors with compliant runners, enabling full control over multiple degrees of freedom and resulting in an L/D ratio higher than that of a conventional, hinged control surface[6,7]. Researchers have reported the possibility of using SMA materials when developing shape-changing devices based on a morphing aerofoil model with a morphing flap to avoid the problem of the discontinuity caused by the operating principle of the traditional rigid aileron equipped with SMA actuators[8]. For instance, in Iyyappan's experiments, SMA was used to modify the upper surface of the aerofoil, obtaining notable results[9]. Kimaru proposed a concept based on an MFC actuator attached to the composite plate that extends along the main wing and connects the leading- and trailing-edge sections. Wind-tunnel tests proved that this conceptual design enhanced the aerodynamic performance[10]. Johannes presented a hybrid morphing wing instrument, actuated using SMAs and MFCs embedded in both surfaces. Not only could the shape of the aerofoil be optimized as a function of the current mission profile, but also the shear layer was influenced[11].

In the above-cited research, the performance of the morphing aerofoil was usually investigated in wind-tunnel experiments, applying techniques such as particle image velocimetry (PIV), pressure measurements and laser Doppler velocimetry, especially for cases based on continuous deformation. PIV measurements were adopted to study the trailing edge of a NACA0012 morphing aileron, to investigate the physical effect on the flow of high-frequency low-amplitude actuation at high Reynolds numbers[12–14]. Abderahmane conducted a numerical investigation of the frequency–amplitude effects of dynamic morphing for a high-lift configuration at a high Reynolds number[15]. Kancharla built a computational model based on finite elements and carried out potential flow computations to obtain the deflection of the upper and lower skins of an aerofoil subjected to aerodynamic pressure and hysteretic deformation of an SMA wire[16]. Szubert reported a conceptual analysis and computational model for how the unsteady buffeting phenomenon develops in the transonic, low-incidence flow around a supercritical aerofoil[17]. Furthermore, he analysed the turbulent flow around a supercritical aerofoil at high Reynolds number and in the transonic regime, involving shock wave–boundary layer interaction and buffet, by employing numerical simulations and turbulence modelling[18].

Against this background, a conceptual hybrid design for an active flow control aerofoil based on SMA and MFC is proposed. CFD simulations are carried out to evaluate the feasibility of the prototype design. In most previous research, the foil is in a static state, which is not appropriate for modelling continuous morphing effects, such as tail vibration. The arbitrary Lagrangian–Eulerian methodology has been utilized recently, but requires greater computational effort and may suffer from data transfer errors during the interaction between the Computer-Aided Engineering (CAE) and CFD computations. Consequently, this work proposes to use the unsteady flow characteristics during dynamic morphing to model vibration, instead of the classical static simulations.

The remainder of this article is organised as follows: The next section introduces the conceptual design, turbulence modelling and CFD model for tail vibration. Secondly, the aerofoil's shape and corresponding aerodynamic performance in three morphing states obtained by the SMA action are obtained. Finally, results investigating the effects of morphing on the aerodynamic performance for different vibration frequencies and amplitudes are presented.

https://doi.org/10.1017/aer.2020.135 Published online by Cambridge University Press

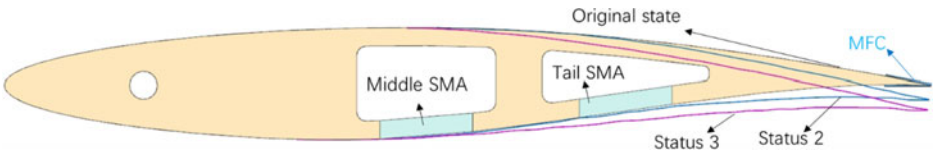

Figure 1. Conceptual design of a hybrid morphing aerofoil (state 1, original state for cruise; state 2, morphing by tail SMA for take-off; state 3, morphing by middle SMA for landing).

2.0 NUMERICAL SIMULATION METHODOLOGY

2.1 Conceptual design

The selected aerofoil is the supercritical RAE2822 foil, whose maximum thickness is 12.1%, located at 37.9% of the chord length, with a maximum curvature of 1.3%, situated at 75.7%c[19]. A hybrid morphing aerofoil is designed based on the SMA driving mechanism for take-off and landing, with MFC actuators for cruise. The SMA-driven deformed wing body is shown in Fig. 1, with two SMA plates embedded in the main body and then encapsulated into an integral active deformation skin by using polydimethylsiloxane[20]. When the pre-stretched SMA plate is energized and heated, its length will decrease, and the restoring force in the SMA plate moves the middle or tail structure of the wing toward the head, thereby achieving bending deformation of the skin. Three aerofoil bending states, including the original form, can be achieved by controlling the states of the middle and tail SMA plates individually. Besides, using the MFCs attached to both sides of the tail substrate, as shown in Fig. 1, a high-frequency and high-precision optimal periodic displacement of the tail can be realized. Reciprocating motion of the tail is achieved by alternately controlling the two groups of MFC to contract and elongate[12].

It is assumed the length of the SMA plates shrinks by 7–10% after temperature changes. Using the mechanical finite-element analysis toolbox Abaqus, the two forms shown in Fig. 1 are obtained under individual action of the rear or middle SMA plate. State 2, with a maximum curvature of 1.87% located at 66.95%, and state 3, with a maximum curvature of 2.1% situated at 72.44%, provide the aerodynamic geometric shape for the subsequent CFD analysis. State 3, with the maximum bending resulting from the middle SMA plate, could be used for landing, while state 2 is used for take-off in line with the requirement in terms of the running conditions of different aircraft.

2.2 Boundary conditions

The inflow boundary condition is the far-field pressure, with a static value of 38.08kPa (A), Mach number of 0.74, AoA of 3.2°, turbulence intensity of 1% and turbulent viscosity ratio of 1. On the solid wall, impermeability and no-slip conditions are applied.

2.3 Turbulence modelling

A density-based algorithm is used to consider the effect of compressibility at high Mach number. The density and viscosity of air are obtained from the ideal gas and Sutherland model, respectively. Considering that the subsequent analysis focuses on the effects of separation and vortex shedding on aerofoil performance, the turbulent model is of great significance[17,21]. Oliviu used the k–ω Shear Stress Transport (SST) model in numerical simulations and validated it for a morphing wingtip at a Mach number of 0.2 and AoA between

https://doi.org/10.1017/aer.2020.135 Published online by Cambridge University Press

Table 1
The lift and drag coefficients for different mesh sizes

Grid	M1	M2	M3	M4
Number	261 000	321 000	445 000	602 000
C_d	0.019	0.018	0.019	0.020
C_l	0.534	0.500	0.477	0.476

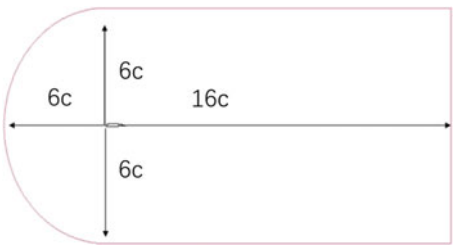

Figure 2. Flowfield geometry configuration.

0° and 5°[22]. In transonic flow research, relevant studies have identified that the two-equation k–ω SST model cannot produce any unsteadiness at the present incidence value, while the Spalart–Almaras model underestimates the amplitudes of the shock motion[15]. Delayed Detached Eddy Simulation (DDES)[23] and Organised Eddy Simulation (OES) k–ε[24,25] are frequently employed for separating flows at small angles of incidence to include the complex interaction between coherent structures and chaotic turbulence. It has been proven that OES k–ε can describe the interaction between transonic buffet and Von Kármán vortices, especially for supercritical aerofoils[26,27]. After careful comparison with the OES k–ε model, DDES is also considered to be a proper model to capture the instability and flow detachment around a supercritical aerofoil[18,28,29]. Therefore, different kinds of turbulence models are adopted herein: k–ω SST is applied when simulating the morphing caused by the SMA at a Mach number of 0.25 and AoA values of 0°, 3.2°, 7° and 10°, while DDES is used to simulate the tail vibration at a Mach number of 0.74 and AoA at 3.2°.

2.4 Numerical parameters

The corresponding numerical simulations are carried out after obtaining the wing's geometric shape under the different bending deformations. The geometric arrangement of the computational model is shown in Fig. 2, with the avoidance of interference from the surrounding boundary. To reduce the mesh scale and computational time requirements, a two-dimensional RAE 2822 aerofoil with a chord length of 0.1m is chosen. The fully structured meshes used for the numerical simulations are generated using ICEM software. A grid convergence study is performed to evaluate the mesh density required to obtain grid-independent values for the aerodynamic coefficients, considering four meshes with 261k, 321k, 445k and 602k elements at Ma 0.74 and an AoA of 3.2°. The mean values of C_l and C_d are presented in Table 1. The numerical results converge, with a difference between M3 and M4 of less than 1% and 5% for C_l and C_d, respectively. Therefore, M3 and its detail is selected for subsequent simulations. Moreover, the grid applied in the present study yields a maximum value of Y plus wall distance of about 0.32, in accordance with the requirement for the turbulence models and ensuring optimal behaviour of the rear turbulent modelling.

https://doi.org/10.1017/aer.2020.135 Published online by Cambridge University Press

Table 2
Time-averaged coefficients for different time steps

Δt	0.5μs	1μs	5μs	10μs
C_l	0.935	0.940	0.935	0.948
C_d	0.109	0.1	0.111	0.128

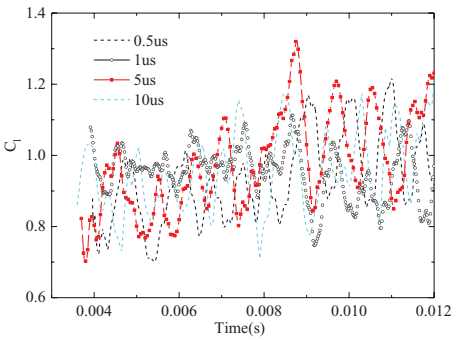

Figure 3. Transient lift coefficient under different time steps.

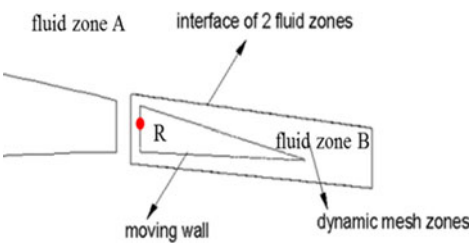

Figure 4. Local fluid domain arrangement.

The suggested time step equation[17] of $5 \times 10^{-4} c/U_\infty$ indicates an appropriate time step (Δt) of about 0.25μs. The time step sensitivity is studied using values of 0.5μs, 1μs, 5μs and 10μs to decrease the computational time requirement. The frequency of fluctuation of C_l in Fig. 3 is similar, while Table 2 indicates that $\Delta t = 10\mu s$ gives a larger average C_l than the other three settings. Therefore, the value of 1μs, which is on the same order as Jean's setting[27], is chosen to obtain accurate results with economic computational effort.

2.5 CFD model for vibration

The above CFD model and settings are adequate to study the static deformation produced by the SMA. However, they cannot be used to model the dynamic morphing of the tail vibration. As a conceptual design to explore the initial instantaneous effect of vibration in terms of flow control, the wing under the action of the MFCs is simplified to the model shown in Fig. 4. The tail is assumed to be separate from the main body and to rotate slightly around the centre point R, located at 95% of the chord, within a specific angular range. For convenience of the CFD study, the fluid domain is divided into two regions. The primary fluid domain A outside of the rectangular frame contains the static mesh, while zone B inside the rectangular frame

https://doi.org/10.1017/aer.2020.135 Published online by Cambridge University Press

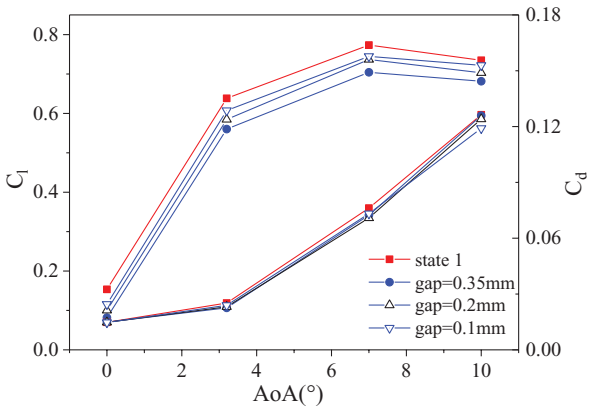

Figure 5. Effect of gap width on C_l and C_d.

contains a dynamic mesh, moving with wall motion. The slit between the tail and the main body must be made as narrow as possible to decrease modelling errors. Based on practical physical instruments, the angular velocity of the vibration is largest at the horizontal position and zero at the upper and lower limit positions. It is reasonable to suppose that the angular velocity of the vibration changes according to the following cosine function:

$$\omega = 2\pi fA \times \cos(2\pi ft) \quad \ldots(1)$$

$$\theta = A \times \sin(2\pi ft) \quad \ldots(2)$$

where f is the vibration frequency, t is time, and A is the vibration amplitude of the tip. In accordance with the gap and length of the tail, A is set to 0.05rad in the subsequent analysis, so that the rotation amplitude in the vertical direction of the wingtip is about 0.25mm. The aerodynamic performance is analysed under different operating conditions by changing the vibration frequency or amplitude.

The aerodynamic performance analyses of the aerofoil model with a slit width of 0.1mm, 0.2mm and 0.35mm are shown in Fig. 5, indicating that the slit width has an apparent influence on the performance of the foil when using the current, simplified model, especially on C_l. With decreasing gap width, the relative error of C_l and C_d compared with the initial results decreases. The maximum error on C_l and C_d is less than 5% for a gap of 0.1mm but 12.2% for a gap of 0.35mm. In subsequent calculations, a slit width of 0.1mm is used. Note that this performance degradation is due to the computational modelling rather than the tail vibration itself. A comparison of C_p along the aerofoil versus experiment results (at $Ma = 0.74$ and $AoA = 3.2°$) is shown in Fig. 6, to evaluate the numerical results. Due to the influence of the gap, the numerical findings are slightly different from the experimental data on the pressure side of the foil. However, the overall results are in agreement with the experiments, confirming the reliability of the model.

3.0 RESULTS OF SMA MORPHING

The C_d and C_l of the aerofoil in the three different bending states for an AoA of 0°, 3.2°, 7° and 10° are analysed at a Mach number of 0.25. The results indicate that C_l increases drastically

https://doi.org/10.1017/aer.2020.135 Published online by Cambridge University Press

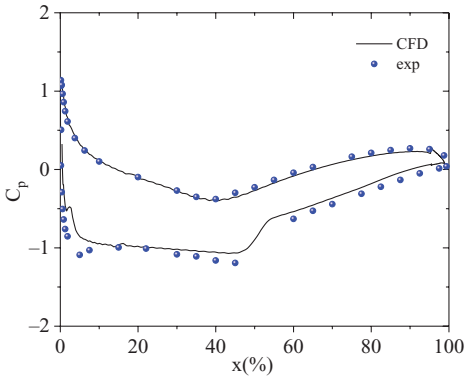

Figure 6. Comparison between numerical results and experimental data (Ma = 0.74, AoA = 3.2°).

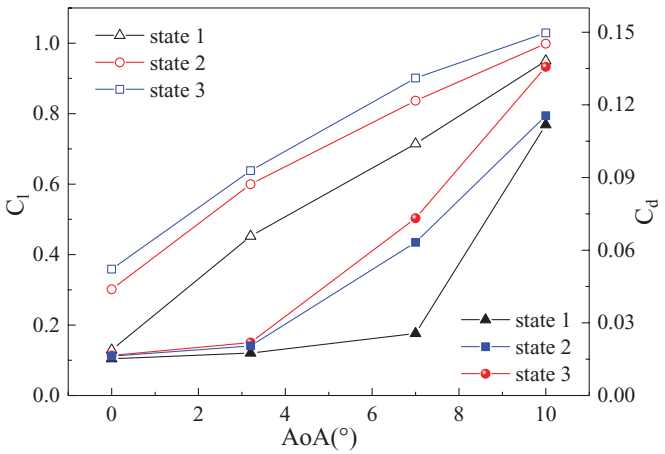

Figure 7. C_l and C_d under different bending morphing and angles of attack (Ma = 0.25).

with beinding of the aerofoil, as shown in Fig. 7 and Table 3. As the middle SMA plate results in significant bending deformation, the lift coefficient in state 3 is the largest when the AoA is smaller than 10°. Also, note that, with increasing AoA, the increasing gradient of C_l is gradually reduced. In state 2 and 3, C_d is always larger than for the original form in Fig. 7, by 146.68% and 185.71% at 7°, respectively. The explanation for this can be seen in Fig. 8, which shows the Root-Mean-Square (RMS) tangential velocity at AoA = 7°.

When the AoA is 7°, the RMS tangential velocity is nearly zero in the original state, suggesting that the flow is steady. However, the flow becomes unsteady in state 2 and 3, with $\Delta v/U_\infty$ reaching 20% and 24%, respectively, according to Fig. 8. Thus, the C_l and C_d in state 2 and 3 are quite different from in the original condition. For state 3, C_l is increased by 26.08%, and C_d by 185.71% compared with state 1. The results for state 2 in Table 3 show that C_l and C_d are both sharply increased. Because of the more drastic bending morphing, the general magnitude of $\Delta v/U_\infty$ in state 3 is larger, leading to the higher C_d.

When the AoA is 10°, the situation is different, with the $\Delta v/U_\infty$ values for the different shapes lying at the same level in Fig. 9, indicating that all the states are unsteady. These results

https://doi.org/10.1017/aer.2020.135 Published online by Cambridge University Press

Table 3
Comparison of C_l and C_d between morphing states and the original state

	State 1		State 3				State 2			
AoA (°)	C_l	C_d	C_l	Ratio	C_d	Ratio	C_l	Ratio	C_d	Ratio
0	0.129	0.015	0.359	177.55%	0.0165	8.82%	0.302	133.40%	0.016	6.84%
3.2	0.452	0.018	0.638	41.06%	0.0219	24.94%	0.600	32.57%	0.020	16.89%
7	0.715	0.026	0.901	26.08%	0.0732	185.71%	0.837	17.11%	0.063	146.68%
10	0.950	0.112	1.029	8.34%	0.1357	21.38%	0.999	5.13%	0.116	3.35%

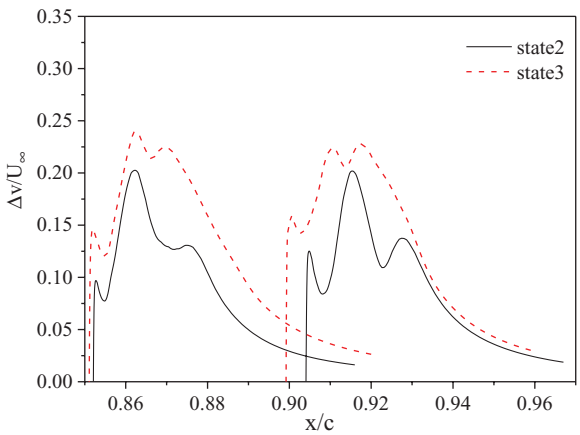

Figure 8. RMS tangential velocity at AoA = 7°.

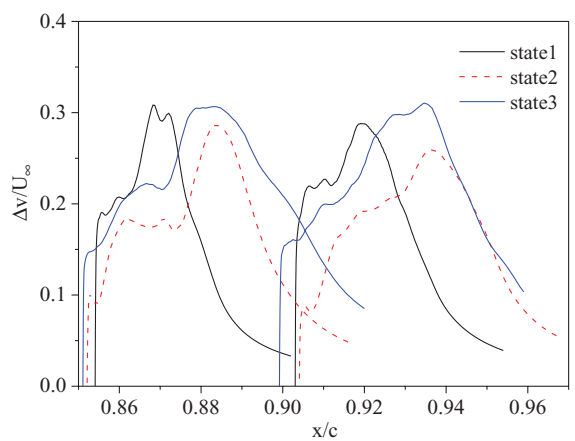

Figure 9. RMS tangential velocity at AoA = 10°.

https://doi.org/10.1017/aer.2020.135 Published online by Cambridge University Press

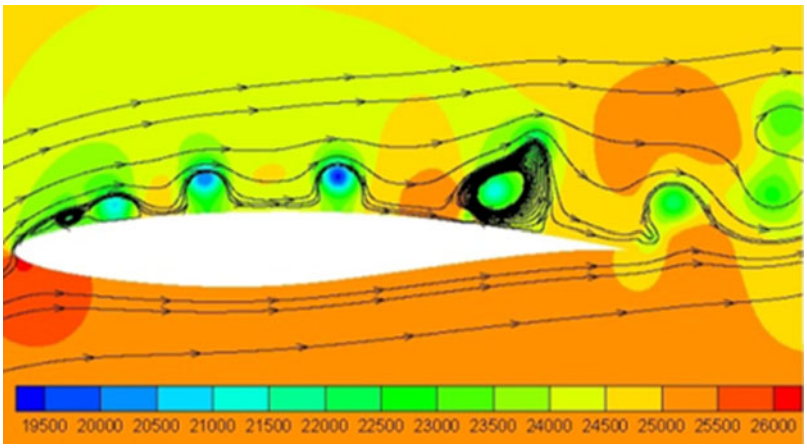

Figure 10. Pressure distribution and streamlines at AoA = 10° in state 1.

are also supported by Fig. 10, where the flow is separated even in state 1. As a result, the difference between the two morphing states and the original form becomes smaller in Table 3, especially for C_d in state 3. The maximum C_d increase is 21.38% in state 3, being significantly smaller than the value of 185.71% obtained at AoA = 7°. Moreover, the percentage increase in C_l dramatically decreases to 8.34% and 5.13% for state 3 and 2, respectively.

4.0 RESULTS OF TAIL VIBRATION BY MFCS

4.1 Effect of vibration frequency

The effects of the frequency and magnitude of the tail vibration are studied at an AoA of 3.2° and a Mach number of 0.74. According to Tian's research[30], the natural transonic buffet frequency of RAE 2822 varies from 60 to 100Hz under different Mach numbers. Therefore, numerical investigations are carried out at various frequencies of 50Hz, 100Hz and 200Hz to explore the impact of the vibration frequency. It is found that C_l is significantly lower than for the original aerofoil in Figs 11 and 12 due to the influence of the slit above. The frequency has a complicated effect on C_l and C_d. C_l shows a peak at $f = 50$Hz, while the minimum C_d occurs at $f = 100$Hz, achieving a decrease of 1.66% compared with the foil at 0Hz in Table 4. It can be inferred that high-frequency vibration of the trailing edge has a more significant influence on C_l than on C_d. Selecting an appropriate frequency could result in an increased ratio of C_l to C_d and meet the aim of decreasing the resistance during the cruise phase. With the tail rotating to the lower limit, the shock wave is strengthened and moves towards the tail direction, while both C_l and C_d start to increase to their maximum simultaneously. When the tail begins rotating upward, the shock wave is compressed, while C_l and C_d move in the opposite direction, as shown in Fig. 13. The vibration significantly locks in the buffet frequency, with C_l, C_d and the shock location being determined by the transient rotation of the tail. C_l reaches its maximum when the tail is at the lower limit. When C_l reaches the bottom limit, the rear is at the upper limit. By changing the frequency of the tail vibration, the buffet frequency of the foil could be changed.

https://doi.org/10.1017/aer.2020.135 Published online by Cambridge University Press

Table 4
C_l and C_d under different vibration frequencies (AoA = 3.2°, Ma = 0.74, A = 0.05)

Frequency	0Hz	50Hz	100Hz	200Hz
C_l	0.592	0.596	0.578	0.583
C_d	0.0302	0.0307	0.0297	0.0301
C_l/C_d	19.603	19.414	19.461	19.369

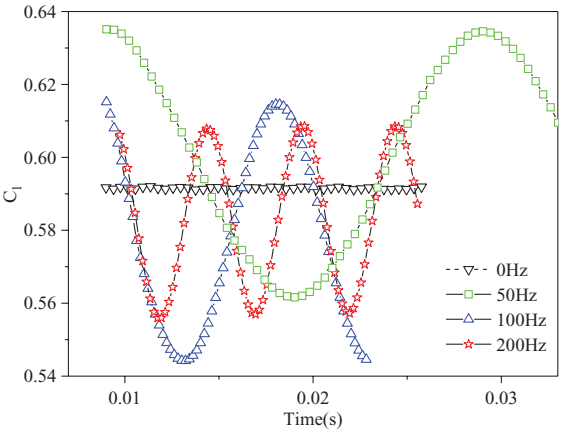

Figure 11. Effect of vibration frequency on C_l.

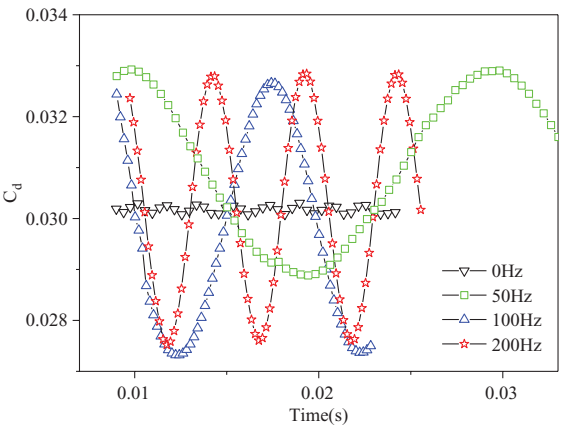

Figure 12. Effect of vibration frequency on C_d.

4.2 Performance under different angles of attack

With an incoming flow at a Mach number of 0.74, the influence of high-frequency vibration of the tail at AoA = 7° is further studied (Fig. 14). The results reveal that the fluctuation of C_l and C_d at 7° is consistent with the description above; That is, the trailing-edge vibration

https://doi.org/10.1017/aer.2020.135 Published online by Cambridge University Press

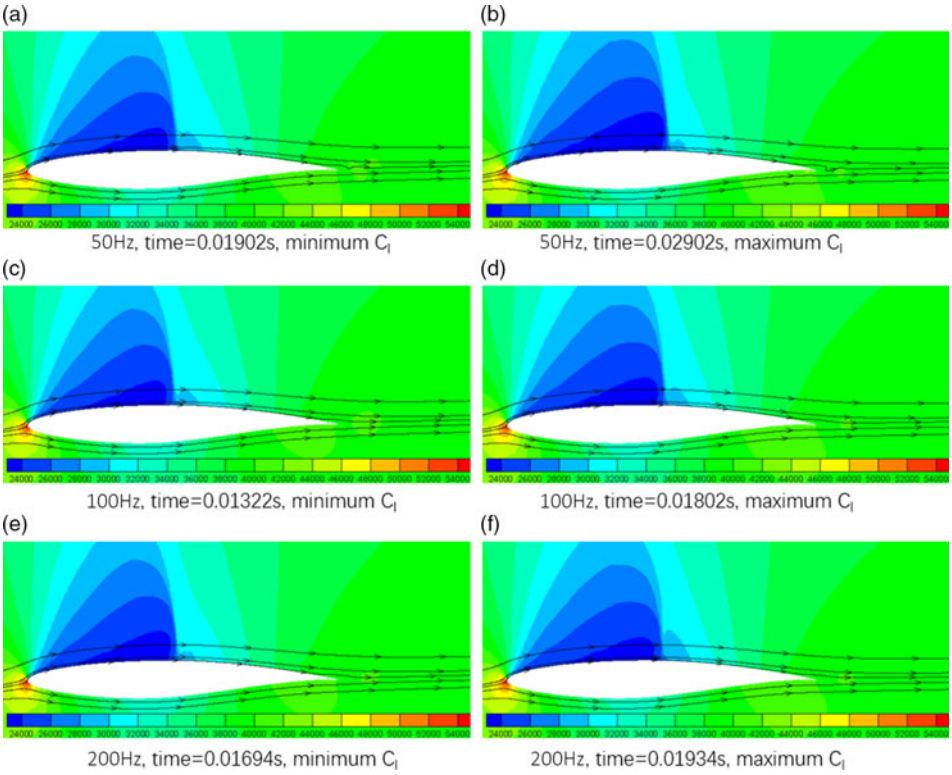

Figure 13. Pressure distribution and streamlines of aerofoil under different frequencies.

reduces the lift and drag coefficients synchronously. At this increased AoA, the amplitude of the fluctuation of C_l and C_d becomes larger. Besides, C_l and C_d undergo two cycles from the maximum to minimum during one period due to the excessive separation. The minimum length of the low-pressure area becomes smaller, as shown in Fig. 15(a), leading to a smaller minimum of C_l, as shown in Fig. 14. Compared with the performance data obtained at 0Hz, C_l decreases by 2.36% and 4.58% at AoA of 3.2° and 7°, respectively, while C_d is reduced by 1.66% and 5.53%, accordingly.

4.3 Effect of vibration amplitude

A in the rotation function above, which is determined by the length and properties of the MFCs, represents different vibration amplitudes. Under the condition with a Mach number of 0.74, AoA of 3.2° and vibration frequency of 100Hz, the performance with a vibration amplitude of $A_0 = 0.05$, $0.75A_0$ and $0.5A_0$ is analysed, and the numerical results are shown in Figs 16 and 17.

As the amplitude of the vibration is decreased, both the mean values of C_l and C_d and the magnitude of the fluctuation decrease due to the influence of the vibration amplitude on both sides of the camber. The lift coefficient increases accordingly due to the camber growth brought about by the tip's moving down, but the effect is reversed when the tail moves

https://doi.org/10.1017/aer.2020.135 Published online by Cambridge University Press

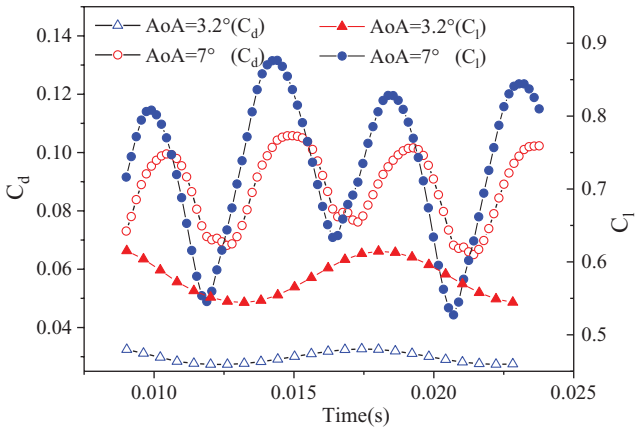

Figure 14. C_d and C_l at different AoA ($f = 100$Hz, $A = 0.05$).

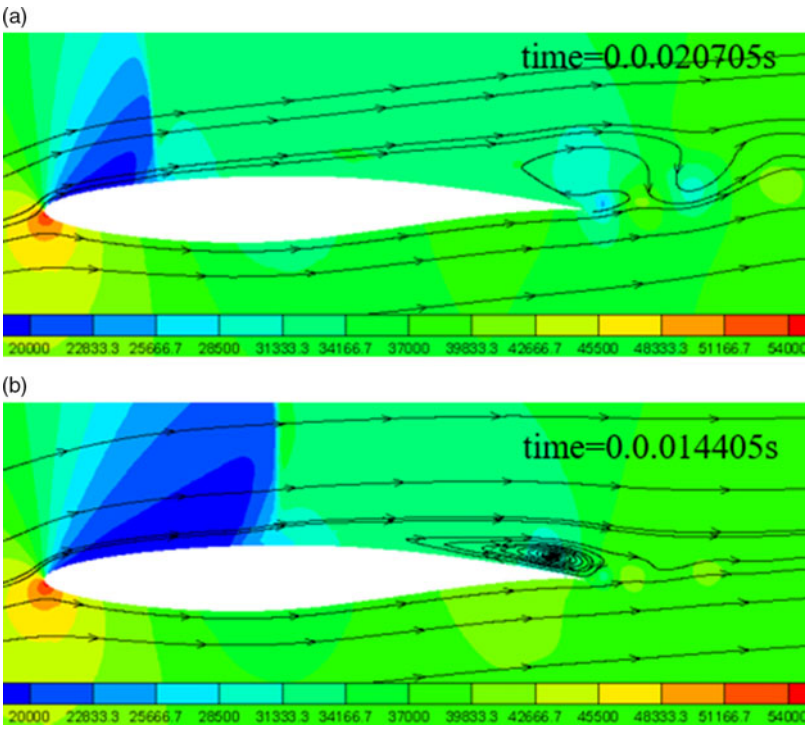

Figure 15. Pressure distribution and streamlines of aerofoil under AoA = 7° (100Hz, A = 0.05).

in the opposite direction. As shown in Table 5, the MFC only slightly changes the time-averaged C_l and C_d values of the aerofoil. Taking the average value for comparison, C_l at $A = 0.5A_0$, $0.75A_0$ and A_0 decreases by 4.7% 3.43% and 2.36% compared with the results without vibration, respectively. The amplitude of the vibration has the same effect on the drag coefficient. The resistance coefficient is decreased by 2.32%, 1.99% and 1.66%, respectively,

https://doi.org/10.1017/aer.2020.135 Published online by Cambridge University Press

Table 5
Time-averaged C_l and C_d under different vibration amplitudes (AoA = 3.2°, Ma = 0.74, f = 100Hz)

Amplitude (A)	A_0 (0Hz)	$0.5A_0$	$0.75A_0$	A_0
C_l	0.592	0.564	0.572	0.578
Percentage decrease	–	4.70%	3.43%	2.36%
C_d	0.0302	0.0295	0.0296	0.0297
Percentage decrease	–	2.32%	1.99%	1.66%
C_l/C_d	19.603	19.119	19.324	19.461

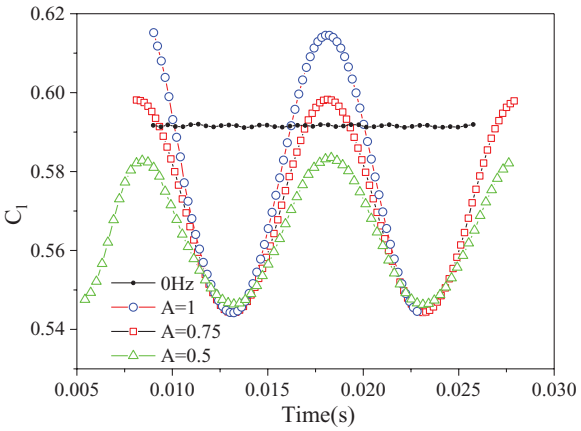

Figure 16. C_l at different vibration amplitudes.

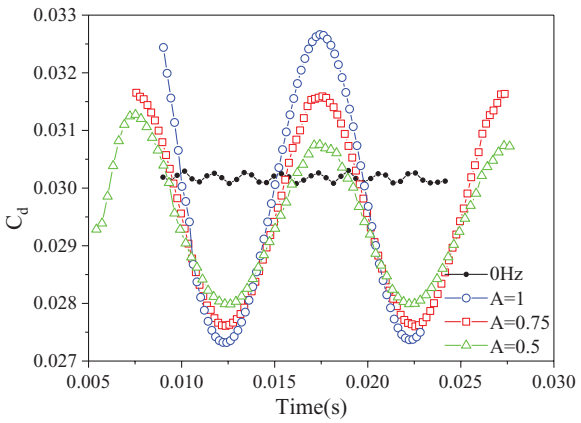

Figure 17. C_d at different vibration amplitudes.

when A is equal to $0.5A_0$, $0.75A_0$ and A_0. On the other hand, the vibration leads C_l and C_d to fluctuate considerably, as also reported by Abderahmane[15] and Jean[27]. Thus, the magnitude and frequency of the tail vibration should be carefully chosen based on the overall design as well as aerodynamic load analysis.

https://doi.org/10.1017/aer.2020.135 Published online by Cambridge University Press

5.0 CONCLUSIONS

The conceptual design for a wing with active flow control based on SMA and MFC is proposed herein. CFD simulations are carried out to evaluate its feasibility to improve the aerodynamic performance. The unsteady flow characteristics with dynamic morphing are investigated instead of classical static simulations with complicated coupling. Furthermore, numerical simulations are applied to analyse the performance under large bending deformation by the action of SMA plates or slight tail vibration applied by MFC at different frequencies, AoAs and vibration amplitudes. The following conclusions can be drawn from the results of the present study.

1. The results of the numerical studies suggest that the proposed conceptual design for a wing with active flow control based on SMA and MFC is feasible to improve the aircraft's aerodynamic performance.
2. The large deformation produced by the SMA plates results in a significant increase in both C_l and C_d, suitable for take-off and landing. In state 3, C_l and C_d are increased by 41.06% and 24.94%, respectively, at an AoA of 3.2°, and by 8.34% and 21.38% at an AoA of 10°, compared with the initial form.
3. The frequency and amplitude have a complicated effect on the performance of the wing under the action of MFCs. C_d decreases by 1.66% at 100Hz, with a simultaneous drop of 2.3% in the time-averaged C_l value. C_d is reduced more when the AoA becomes larger, with the decrease reaching 5.53% for an AoA at 7°. In conclusion, a decrease of C_d on the order of 1.66–2.32% is achieved when choosing an appopriate frequency and amplitude for cruise.

REFERENCES

1. WASHBURN, A., GORTON S. and ANDERS, S. A Snapshot of active flow control research at NASA Langley. In 1st flow control conference, American Institute of Aeronautics and Astronautics: St. Louis, Missouri, 2002.
2. SCOTT, C.S., JOSLIN, R.D., SEIFERT, A. and THEOFILIS, V. Issues in active flow control: theory, control, simulation, and experiment. *Prog Aerosp Sci.* 2004, **40**, (4–5), pp 237–289.
3. KHAN, S., GRIGORIE, T.L., BOTEZ, R., MAMOU, M. and MÉBARKI, Y. Novel morphing wing actuator control-based particle swarm optimisation. *Aeronaut J.* 2019, **124**, (1271), pp 1–21.
4. MALDONADO, V., FARNSWORTH, J., GRESSICK, W. and AMITAY, M. Active control of flow separation and structural vibrations of wind turbine blades. *Wind Energy.* 2010, **13**, (2–3), pp 221–237.
5. BOTEZ, R.M., KAMMEGNE, M.J.T. and GRIGORIE, L.T. Design, numerical simulation and experimental testing of a controlled electrical actuation system in a real aircraft morphing wing model. *Aeronaut J.* 2015, **119**, (1219), pp 1047–1072.
6. WU, R., COSTAS, S., ZHONG S. and FILIPPONE A. A morphing aerofoil with highly controllable aerodynamic performance. *Aeronaut J.* 2017, **121**, (1235), pp 54–72.
7. BAIER, H. and DATASHVILI, L. Active and morphing aerospace structures-a synthesis between advanced materials, structures and mechanisms. *Int J Aeronaut Space Sci.* 2011, **12**, (3), pp 225–240.
8. BOTEZ, R.M., KOREANSCHI, A., GABOR, O.S., TONDJI, Y., GUEZGUEZ, M., KAMMEGNE, J.T., GRIGORIE, L.T. and SANDU, D. Numerical and experimental transition results evaluation for a morphing wing and aileron system. *Aeronaut J.* 2018, **122**, (1251), pp 747–784.
9. IYYAPPAN, B. Numerical and experimental investigation on aerodynamic characteristics of SMA actuated smart wing model. *Int J Eng Technol.* 2013, **5**, (5), pp 3813–3818.
10. KIMARU, J. and BOUFERROUK, A. Design, manufacture and test of a camber morphing wing using MFC actuated smart rib. In 2017 8th international conference on mechanical and aerospace engineering (ICMAE), IEEE: Prague, Czech Republic. 2017, pp 791–796.

https://doi.org/10.1017/aer.2020.135 Published online by Cambridge University Press

11. SCHELLER, J., JODIN, G., RIZZO, K.J., DUHAYON, E., ROUCHON, J.F., TRIANTAFYLLOU, M.S. and BRAZA, M. A combined smart-materials approach for next-generation airfoils. *Solid State Phenomena.* 2016, **251**, pp 106–112.
12. JODIN, G., MOTTA, V., SCHELLER, J., DUHAYON, E., DÖLL, C., ROUCHON, J.F. and BRAZA, M. Dynamics of a hybrid morphing wing with active open loop vibrating trailing edge by time-resolved PIV and force measures. *J Fluids Struct.* 2017, **74**, pp 263–290.
13. SCHELLER, J., CHINAUD, M., ROUCHON J., DUHAYON, E., CAZIN, S., MARCHAL, M. and BRAZA, M. Trailing-edge dynamics of a morphing NACA0012 aileron at high Reynolds number by high-speed PIV. *J Fluids Struct.* 2015, **55**, pp 42–51.
14. CHINAUD, M., ROUCHON, J., DUHAYON, E., SCHELLER, J., CAZIN, S., MARCHAL, M. and BRAZA, M. Trailing-edge dynamics and morphing of a deformable flat plate at high reynolds number by time-resolved PIV. *J Fluids Struct.* 2014, **47**, pp 41–54.
15. ABDERAHMANE, M., JEAN, B.T., JEAN, F.R., YANNICK, H. and BRAZA, M. Numerical investigation of frequency-amplitude effects of dynamic morphing for a high-lift configuration at high Reynolds number. *Int J Numer Methods Heat Fluid Flow.* 2019, ahead-of-print.
16. KANCHARLA, A.K. and ROY, M. Aerodynamic pressure variation over SMA wire integrated morphing aerofoil. In 49th AIAA/ASME/ASCE/AHS/ASC Structures, Structural Dynamics, and Materials Conference, Schaumburg, IL, 2008.
17. SZUBERT, D., GROSSI, F., JIMENEZ, G., HOARAU, Y., HUNT, J.C.R. and BRAZA, M. Shock-vortex shear-layer interaction in the transonic flow around a supercritical airfoil at high Reynolds number in buffet conditions. *J Fluids Struct.* 2015, **55**, pp 276–302.
18. SZUBERT, D., ASPROULIAS, I., GROSSI, F., DUVIGNEAU, R., HOARAU, Y. and BRAZA, M. Numerical study of the turbulent transonic interaction and transition location effect involving optimisation around a supercritical aerofoil. *Eur J Mech B/Fluids.* 2016, **55**, pp 380–393.
19. COOK, P., MCDONALD, H.M.A. and FIRMIN, M.C.P. Airfoil RAE 2822 pressure distributions and boundary layer and wake measurements, Experimental data base for computer program assessment, AGARD report AR138,1979.
20. HARTL, D.J., LEAL, P. and STROUD, H.R. Experimental multiphysical characterization of an SMA driven, camber morphing owl wing section. In Nondestructive Characterization and Monitoring of Advanced Materials, Aerospace, Civil Infrastructure, and Transportation XII, Shull, P J, Ed, SPIE: Denver, United States, 2018, pp 36–44.
21. HAN, X., KRAJNOVIĆ, S. and BASARA, B. Study of active flow control for a simplified vehicle model using the PANS method. *Int J Heat Fluid Flow.* 2013, **42**, pp 139–150.
22. OLIVIU, S.G., ANDREEA, K., RUXANDRA, M.B., MAHMOUD, M. and YOUSSEF, M. Numerical simulation and wind tunnel tests investigation and validation of a morphing wing-tip demonstrator aerodynamic performance. *Aerosp Sci Technol.* 2016, **53**, pp 136–153.
23. SHINDE, V., MARCEL, T., HOARAU, Y., *et al.* Numerical simulation of the fluid–structure interaction in a tube array under cross flow at moderate and high Reynolds number. *J Fluids Struct.* 2014, **47**, pp 99–113.
24. BRAZAA, M., PERRINA, R. and HOARAU, Y. Turbulence properties in the cylinder wake at high Reynolds numbers. *J Fluids Struct.* 2006, **22**, pp 757–771.
25. BOURGUET, R., BRAZA, M., HARRAN, G. and AKOURY, R.E. Anisotropic Organised Eddy Simulation for the prediction of non-equilibrium turbulent flows around bodies. *J Fluids Struct.* 2008, **24**, (8), pp 1240–1251.
26. SIMIRIOTIS, N., JODIN, G., MAROUF, A., ELYAKIME, P., HOARAU, Y., HUNT, J.C.R., ROUCHON, J.F. and BRAZA, M. Morphing of a supercritical wing by means of trailing edge deformation and vibration at high Reynolds numbers: Experimental and numerical investigation. *J Fluids Struct.* 2019, **91**, p 102676.
27. JEAN, B.T., SIMIRIOTIS, N., MAROUF, A., SZUBERT, D., ASPROULIAS, I., ZILLI, D.M., HOARAU, Y., HUNT, J.C.R. and BRAZA, M. Effects of vibrating and deformed trailing edge of a morphing supercritical airfoil in transonic regime by numerical simulation at high Reynolds number. *J Fluids Struct.* 2019, **91**, p 102595.
28. MAROUF, A., HOARAU, Y., VOS, J.B., CHARBONNIER, D. and TEKAP, Y.B. Evaluation of the aerodynamic performance increase thanks to a morphing A320 wing with high-lift flap by means of CFD Hi-Fi approaches. AIAA Aviation 2019 Forum. Dallas, Texas, 2019.

https://doi.org/10.1017/aer.2020.135 Published online by Cambridge University Press

29. BARBUT, G., BRAZA, M., HOARAU, Y., BARAKOS, G., SÉVRAIN, A. and VOS, J.B. Prediction of transonic buffet around a wing with flap. Progress in Hybrid RANS-LES Modelling. Berlin: Springer. 2010, pp 191–204.
30. TIAN, Y., GAO, S.Q., LIU, P.Q. and WANG, J.J. Transonic buffet control research with two types of shock control bump based on RAE2822 airfoil. *Chinese J Aeronaut.* 2017, **30**, (5), pp 1681–1696.

https://doi.org/10.1017/aer.2020.135 Published online by Cambridge University Press